TU Delft

Delft University of Technology

Position and Orientation Estimation Uncertainty Using Magnetometer Arrays for Indoor Localization

Edridge, T.I.; Kok, M.

DOI
10.1109/JISPIN.2025.3567258

Licence
CC BY

Publication date
2025

Document Version
Final published version

Published in
IEEE Journal of Indoor and Seamless Positioning and Navigation

Citation (APA)
Edridge, T. I., & Kok, M. (2025). Position and Orientation Estimation Uncertainty Using Magnetometer Arrays for Indoor Localization. *IEEE Journal of Indoor and Seamless Positioning and Navigation* , *3*, 152-164. https://doi.org/10.1109/JISPIN.2025.3567258

Important note
To cite this publication, please use the final published version (if applicable).
Please check the document version above.

Copyright
Other than for strictly personal use, it is not permitted to download, forward or distribute the text or part of it, without the consent of the author(s) and/or copyright holder(s), unless the work is under an open content license such as Creative Commons.

Takedown policy
Please contact us and provide details if you believe this document breaches copyrights.
We will remove access to the work immediately and investigate your claim.

This work is downloaded from Delft University of Technology.
For technical reasons the number of authors shown on this cover page is limited to a maximum of 10.

Position and Orientation Estimation Uncertainty Using Magnetometer Arrays for Indoor Localization

Thomas Edridge, *Graduate Student Member, IEEE*, and Manon Kok

***Abstract*—Recently, it has been shown that odometry is possible only using data from a magnetometer array. In this work, we analyze the uncertainty of the pose change estimate using a magnetometer array. We derive an analytical expression for the pose change covariance to analyze the estimation uncertainty in Monte Carlo simulations. Under certain conditions, we demonstrate that using a magnetometer array, it is possible to estimate the position and orientation change with submillimeter and subdegree precision between two consecutive time-steps. Moreover, we also demonstrate that when constructing a magnetometer array, magnetometers should be placed in the direction of movement to maximize the positional and rotational precision, with at least four magnetometers per unit of length-scale. In addition, we illustrate that to minimize positional and rotational drift to under a few percentages and degrees of the distance traveled, submillimeter and subdegree magnetometer alignment errors are necessary. Similarly, bias errors smaller than a few percent of the magnitude of the magnetic field variations are necessary. The Monte Carlo simulations are verified using experimental data collected with a 30-magnetometer array. The experimental data show that when insufficient magnetic field anomalies are in close proximity, the changes in positions are estimated poorly, while significant orientation information is still obtained. It also shows that when the magnetometer array is in close proximity to sufficient magnetic field anomalies, the overall trajectory traveled by a magnetometer array can be accurately estimated with a horizontal error accumulation of less than a percentage of the distance traveled.**

***Index Terms*—Gaussian process (GP), indoor localization, magnetic field, magnetometer, sensor array.**

I. Introduction

INDOOR localization is challenging as the Global Navigation Satellite System (GNSS) signal is attenuated in indoor environments, rendering it unusable for submeter positional precision [1]. Yet, the growing need for indoor localization can be seen in, e.g., emergency response situations [2], robots [3], medicine [4], [5], augmented reality [6], and many more. As such, indoor localization is an active research field [7], [8], [9]. Indoor localization systems commonly use an inertial measurement unit, which includes an accelerometer and a gyroscope; however, when used independently, these sensors suffer from positional and rotational drift [10]. Additional sensors, such as acoustic, optical, or radio frequency systems, can be used to minimize drift. Unfortunately, these methods often require either infrastructure or line-of-sight [11]. Recent research has focused on utilizing the magnetic field as a source for indoor localization, which is cost-effective and does not require line-of-sight or dedicated infrastructure.

Although the magnetic field has shown great potential for indoor localization [12], [13], [14], [15], [16], [17], most works only use a single magnetometer to improve the heading estimate by using the Earth's magnetic field as a compass. Alternatively, anomalies are present in the magnetic field, which are created by ferromagnetic materials present within the structure of buildings [10]. These anomalies can be incorporated into a magnetic field map and can be used for position and orientation estimation. This may require the map to be known *a priori* see, e.g., [18]. Alternatively, the magnetic field map can be learned simultaneously with the position and orientation. However, this necessitates a revisitation of a previously visited location along the taken trajectory [17]. The dependency on revisitations limits the exploration time and/or space when mapping out new areas.

Fortunately, in recent years, an alternative line of research has looked into using a magnetometer array, i.e., multiple magnetometers connected by rigid body constraints. It has been shown that using multiple magnetometers yields significantly more information [19], [20], [21], [22], [23], [24], [25], [26]. In fact, using magnetometer measurements from a single time step, a local magnetic field map around the magnetometers of the array can be constructed from which, it is shown in [24] and [25], that odometry is possible. An example of this is illustrated in Fig. 1.

A magnetometer array was first used to provide information about the change in position in [19], where they show that velocity estimates can be obtained using an array of spatially

Received 22 January 2025; revised 13 March 2025 and 18 April 2025; accepted 28 April 2025. Date of publication 6 May 2025; date of current version 20 May 2025. This work was supported in part by the Project "Sensor Fusion For Indoor Localisation Using The Magnetic Field" under Project 18213 of the Research Program Veni, funded by the Dutch Research Council (NWO) and in part by Sensor AI Lab, through the AI Labs Program of Delft University of Technology. *(Corresponding author: Thomas Edridge.)*

The authors are with the Delft Center for Systems and Control (DCSC), Delft University of Technology, 2628 CD Delft, The Netherlands (e-mail: t.i.edridge@tudelft.nl; m.kok-1@tudelft.nl).

Data is available online at https://github.com/Tedridge/magnetometerArrayOdometryAnalysis.

Digital Object Identifier 10.1109/JISPIN.2025.3567258

© 2025 The Authors. This work is licensed under a Creative Commons Attribution 4.0 License. For more information, see https://creativecommons.org/licenses/by/4.0/

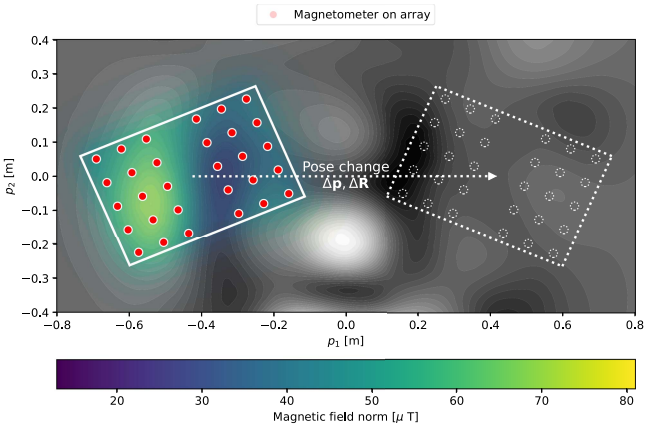

Fig. 1. Example of the ambient magnetic field norm in an indoor environment with data collected using a 30-magnetometer array. Anomalies in the magnetic field can be seen with the magnetic field norm ranging from $[15, 80]$ μT. The 30 magnetometers are placed in a plane, and the movement of the pose (position and rotation) change is in-plane. In color is where the measurements before the array provide information about the magnetic field. The dotted outline illustrates the location of a possible pose change.

distributed magnetometers. The velocity is estimated by including magnetic field gradient information, which is estimated by exploiting the information that magnetometers are placed on an array. The authors follow up on this work in [20], [21], [22], [23], and [27]. Inspired by this work, the authors of [24] and [25] estimated the pose change directly rather than estimating velocity. In these works, a method for magnetic field-only odometry based on the magnetometer is proposed, and we directly build on this work. The pose change $\{\Delta\mathbf{p}, \Delta\mathbf{R}\}$, which contains the change in position $\Delta\mathbf{p}$ and orientation $\Delta\mathbf{R}$, is estimated in [25] by solving the weighted Euclidean norm as follows:

$$\Delta\hat{\mathbf{p}}, \Delta\hat{\mathbf{R}} = \arg\min_{\Delta\mathbf{p},\mathbf{R}} V(\Delta\mathbf{p}, \Delta\mathbf{R}). \tag{1}$$

Building on this work, the authors in [28] and [29] combined the magnetometer array with an inertial navigation system. Both works demonstrate a significant error reduction compared to stand-alone inertial navigation systems.

Currently, there are a lot of open questions on using a magnetometer array for indoor localization. To give more insight, this article provides the following contributions.

1) We derive an analytical expression for the pose change covariance to analyze the quality of odometry, where we build on the pose change solution derived in [25]. We use the covariance to analyze the odometry precision in a Monte Carlo (MC) simulation when we move at different speeds in the in-plane and out-of-plane directions using a magnetometer array. We analyze the precision of odometry by altering the size of the magnetometer array. Furthermore, we analyze the odometry precision if the configuration of the magnetometer array changes—whether in a line, a plane, or a cube. Finally, we analyze the odometry under the effects of different magnetometer noise levels, magnetometer biases, and misalignment errors.
2) To validate the simulation results, we conduct an experiment in which the pose change of a 30-magnetometer array is estimated while taking steps of varying lengths in the in-plane direction. We also demonstrate the efficacy of magnetic field odometry using experimental data, where the array is moved along 2-D trajectories: a small square at ground height, and a large square at knee and head heights.

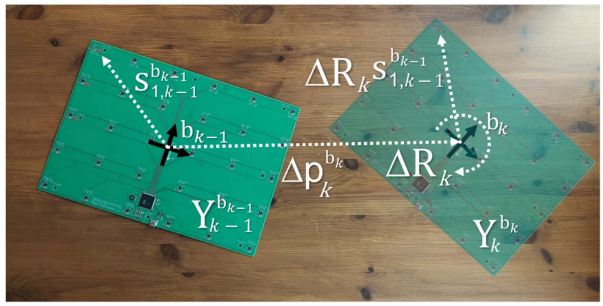

Fig. 2. Photograph of a 30-magnetometer array of size 0.32 m $\times$ 0.22 m. The magnetometers are RM3100 from PNI running at 500 Hz. The body frame is attached to the center of the magnetometer array at every time-step k. A possible pose change $\{\Delta\mathbf{p}^{\mathrm{b}_k}_k, \Delta\mathbf{R}_k\}$ is shown with a transparent overlay. The location of the first magnetometer is shown before and after the pose change.

Knowledge of the covariance of the pose change and minimizing it is important, as even if the estimation errors of the pose change are small, they will quickly add up over time.

II. Method

We are interested in estimating the pose change of a magnetometer array. To this end, we introduce a moving coordinate frame b_k, aligned with the center of the magnetometer array at each time step k as shown in Fig. 2. As we assume the magnetometers are subject to rigid body constraints, the relative distances between magnetometers are fixed and assumed to be known in this frame. The magnetometers are aligned with this frame and measure the magnetic field, from which local magnetic field predictions can be made, as illustrated in Fig. 1.

Similar to [25], we estimate the pose change by solving the nonlinear optimization problem (1) with

$$V(\Delta\mathbf{p}^{\mathrm{b}_k}_k, \Delta\mathbf{R}_k) = ||\Delta\mathbf{R}^{\mathsf{T}}_k\mathbf{Y}^{\mathrm{b}_k}_k - f(\Delta\mathbf{P}^{\mathrm{b}_k}_k + \Delta\mathbf{R}_k\mathbf{S}^{\mathrm{b}_{k-1}})||^2_{\mathbf{\Sigma}^{-1}_{V,k}}. \tag{2}$$

where $\mathbf{Y}^{\mathrm{b}_k}_k$ are the magnetometer array measurements after the pose change at time-step k, $f(\cdot)$ is a probabilistic nonlinear function, which predicts the magnetic field values. Furthermore, $\mathbf{S}^{\mathrm{b}_k}$ denotes all the magnetometer locations on the array in the body frame. Finally, $\mathbf{\Sigma}^{-1}_V(\Delta\mathbf{p}^{\mathrm{b}_k}_k, \Delta\mathbf{R}_k)$ (denoted $\mathbf{\Sigma}^{-1}_{V,k}$ for brevity) is the uncertainty of the probabilistic model $f(\cdot)$ and the covariance of the magnetometers measurements. We are interested in finding the covariance of the pose change $\mathbf{\Sigma}_{\boldsymbol{\zeta},k}$, which is given in [30] as follows:

$$\mathbf{\Sigma}_{\boldsymbol{\zeta},k} \approx \hat{\lambda}_k \left(\boldsymbol{\mathcal{J}}^{\mathsf{T}}_{\boldsymbol{\zeta},k}\mathbf{\Sigma}^{-1}_{V,k}\boldsymbol{\mathcal{J}}_{\boldsymbol{\zeta},k}\right)^{-1} \tag{3}$$

with $\hat{\lambda}_k = V(\Delta\mathbf{p}^{\mathrm{b}_k}_k, \Delta\mathbf{R}_k)/(3\text{ m})$, where m is the number of magnetometers. Furthermore, $\boldsymbol{\zeta}$ is the error of the pose change, to be defined in Section II-B. Our contribution lies in the analytical

derivation of $\boldsymbol{\Sigma}_{\boldsymbol{\zeta},k}$, for which we will derive $\boldsymbol{\Sigma}_{V,k}$ and $\boldsymbol{\mathcal{J}}_{\boldsymbol{\zeta},k}$. This will be used for this article's main goal: To analyze the quality of the pose change. To this end, we first introduce how predictions of the ambient magnetic field can be made using Gaussian process (GP) regression with the curl-free assumption from [31] in Section II-A, Afterward, we introduce the rigid body constraint assumption, which is necessary to relate all magnetometer locations to a single change position $\Delta\mathbf{p}_k^{\mathsf{b}_k}$ and rotation $\Delta\mathbf{R}_k$ for every time step. This allows us to set up the cost function from (2) to find the pose change. Afterward, we demonstrate how to find the Jacobian $\boldsymbol{\mathcal{J}}_{\boldsymbol{\zeta},k}$ of the residual in (2) in Section II-B, which is used to find an analytical expression of the covariance of the pose change. In Section II-C, we use the covariance expression to describe Algorithm 1, where we analyze the pose change estimation precision in different MC simulations.

A. Measurement Model of a Magnetometer Array With Rigid Body Constraints

We model the magnetic field using a latent function $f(\cdot)$, for which we choose GP regression. A GP is uniquely defined by a mean function $m(\mathbf{p})$ and a chosen covariance function $\kappa(\mathbf{p},\mathbf{p}')$ [32]. We choose to model the GP and a covariance function as the sum of a constant kernel $\kappa_{\text{con}}(\mathbf{p},\mathbf{p}') = \sigma_{\text{con}}^2\mathbf{I}_3$, where $\mathbf{I}$ denotes the identity matrix, and the kernel with the curl-free assumption from [31] as follows:

$$f(\mathbf{p}) \sim \mathcal{GP}\left(\mathbf{0}_3, \kappa_{\text{con}}(\mathbf{p},\mathbf{p}') + \kappa_{\text{cf}}(\mathbf{p},\mathbf{p}')\right). \tag{4}$$

The curl-free kernel assumption ensures that the Maxwell equations are satisfied, which has shown to be effective for modeling the magnetic field as a curl-free vector field [16]. The constant kernel accounts for the Earth's magnetic field, and the curl-free kernel accounts for anomalies present in indoor environments. The curl-free kernel is given as follows:

$$\kappa_{\text{cf}}(\mathbf{p},\mathbf{p}') = \sigma_f^2\left(\mathbf{I}_3 - \frac{(\mathbf{p}-\mathbf{p}')(\mathbf{p}-\mathbf{p}')^{\mathsf{T}}}{l^2}\right) \exp\left(\frac{||\mathbf{p}-\mathbf{p}'||^2}{-2l^2}\right) \tag{5}$$

where we have the hyperparameter σ_f^2, which denotes the signal variance, and l, which denotes the length-scale. Based on our model of the magnetic field, we have the following measurement equation:

$$\mathbf{y}_{i,k}^{\mathsf{b}_k} = f(\mathbf{p}_{i,k}^{\mathsf{b}_k}) + \mathbf{e}_{i,k}^{\mathsf{b}_k}, \quad \mathbf{e}_{i,k}^{\mathsf{b}_k} \sim \mathcal{N}(0, \sigma_{\text{y}}^2\mathbf{I}_3) \tag{6}$$

where $\mathbf{y}_{i,k}^{\mathsf{b}_k} \in \mathbb{R}^3$ is the measurement of magnetometer i at time step k. As we are interested in the pose change of the magnetometer array, we make the following assumptions: we assume a magnetometer array with $i = 1,\ldots,m$ magnetometers. The body frame at every time-step is fixed to the center of the array, which allows us to write every magnetometer location as $\mathbf{p}_{i,k-1}^{\mathsf{b}_{k-1}} = \mathbf{s}_i^{\mathsf{b}_{k-1}}$, where $\mathbf{s}_i^{\mathsf{b}_{k-1}}$ is the displacement from the center to magnetometer i. We assume that the displacements $\mathbf{s}_i^{\mathsf{b}_{k-1}}$ are constant and known. We may then write the magnetometer position of the current time-step k in terms of a change in position as $\Delta\mathbf{p}_k$ and rotation $\Delta\mathbf{R}_k$ as $\mathbf{p}_{i,k}^{\mathsf{b}_k} = \Delta\mathbf{p}_k^{\mathsf{b}_k} + \Delta\mathbf{R}_k\mathbf{s}^{\mathsf{b}_{k-1}}$, as illustrated in Fig. 2. We can then concatenate the magnetometer locations as follows:

$$\mathbf{P}_k^{\mathsf{b}_k} = \Delta\mathbf{P}_k^{\mathsf{b}_k} + \Delta\mathbf{R}_k\mathbf{S}^{\mathsf{b}_{k-1}} \tag{7}$$

where matrix $\mathbf{S}^{\mathsf{b}_k}$ contains the displacements $\mathbf{s}_i^{\mathsf{b}_{k-1}}$ from the array's origin to the magnetometers as $\mathbf{S}^{\mathsf{b}_{k-1}} = \begin{bmatrix}\mathbf{s}_1^{\mathsf{b}_{k-1}} & \ldots & \mathbf{s}_m^{\mathsf{b}_{k-1}}\end{bmatrix}$ from before the pose change. Furthermore, $\Delta\mathbf{P}_k^{\mathsf{b}_k} = \mathbf{1}_m^{\mathsf{T}} \otimes \Delta\mathbf{p}_k^{\mathsf{b}_k}$ is the array's change of the array location m times. Here, $\mathbf{1}$ denotes a vector of ones and $\otimes$ denotes the Kronecker product. The matrix dimensions of $\Delta\mathbf{P}_k^{\mathsf{b}_k}$ are $\mathbb{R}^{3\times m}$.

Each magnetometer measures a noisy 3-D vector of the magnetic field at its current location. We concatenate the m magnetometer measurements together at time-step k as $\mathbf{Y}_k^{\mathsf{b}_k} = \begin{bmatrix}\mathbf{y}_{1,k}^{\mathsf{b}_k} & \ldots & \mathbf{y}_{m,k}^{\mathsf{b}_k}\end{bmatrix} \in \mathbb{R}^{3\times m}$, so we can write the measurement equations for m magnetometers on the array as follows:

$$\mathbf{Y}_k^{\mathsf{b}_k} = \Delta\mathbf{R}_k f(\Delta\mathbf{P}_k^{\mathsf{b}_k} + \Delta\mathbf{R}_k\mathbf{S}^{\mathsf{b}_{k-1}}) + \mathbf{E}_{\text{y},k}^{\mathsf{b}_k}. \tag{8}$$

The matrix $\mathbf{E}_{\text{y},k}^{\mathsf{b}_k} = \begin{bmatrix}\mathbf{e}_{\text{y},1,k}^{\mathsf{b}_k} & \ldots & \mathbf{e}_{\text{y},m,k}^{\mathsf{b}_k}\end{bmatrix} \in \mathbb{R}^{3\times m}$ contains all magnetometer measurement errors with covariance

$$\boldsymbol{\Sigma}_{\mathbf{e}_\text{y}} = \text{blockdiagonal}\left(\boldsymbol{\Sigma}_{\mathbf{e}_{\text{y},1}}, \ldots, \boldsymbol{\Sigma}_{\mathbf{e}_{\text{y},m}}\right) \tag{9}$$

where $\boldsymbol{\Sigma}_{\mathbf{e}_{\text{y},i}}$ is the covariance of magnetometer i.

We can use measurement (8) to make predictions of the magnetic field at the magnetometer locations after the pose change. The predictive equations for GPs $f(\mathbf{P}_k^{\mathsf{b}_k}) \sim \mathcal{N}(\boldsymbol{\mu}_k, \boldsymbol{\Sigma}_k)$, as given in [32], are as follows:

$$\begin{aligned}\boldsymbol{\mu}_k &= \mathbf{K}_{k,k-1}\left(\mathbf{K}_{k-1,k-1} + \sigma_{\text{y}}^2\mathbf{I}_{3m}\right)^{-1}\text{vec}(\mathbf{Y}_{k-1}^{\mathsf{b}_{k-1}}) \\ \boldsymbol{\Sigma}_k &= \mathbf{K}_{k,k} - \mathbf{K}_{k,k-1}\left(\mathbf{K}_{k-1,k-1} + \sigma_{\text{y}}^2\mathbf{I}_{3m}\right)^{-1}\mathbf{K}_{k-1,k}\end{aligned} \tag{10}$$

where we have made use of the substitutions $\mathbf{K}_{k-1,k-1} = \mathbf{K}(\mathbf{S}^{\mathsf{b}_{k-1}}, \mathbf{S}^{\mathsf{b}_{k-1}})$, $\mathbf{K}_{k,k-1} = \mathbf{K}(\Delta\mathbf{P}_k^{\mathsf{b}_k} + \Delta\mathbf{R}_k\mathbf{S}^{\mathsf{b}_{k-1}}, \mathbf{S}^{\mathsf{b}_{k-1}})$, and $\mathbf{K}_{k,k} = \mathbf{K}(\Delta\mathbf{P}_k^{\mathsf{b}_k} + \Delta\mathbf{R}_k\mathbf{S}^{\mathsf{b}_{k-1}}, \Delta\mathbf{P}_k^{\mathsf{b}_k} + \Delta\mathbf{R}_k\mathbf{S}^{\mathsf{b}_{k-1}})$ for notational simplicity. The kernel matrix $\mathbf{K}(\cdot,\cdot)$ is generated by evaluating the kernel functions $\kappa_{\text{con}}(\cdot,\cdot) + \kappa_{\text{cf}}(\cdot,\cdot)$ for a corresponding amount of input pairs. The notation $\text{vec}(\cdot)$ shapes a matrix of size $\mathbb{R}^{3\times m}$ into a vector of $\mathbb{R}^{3m\times 1}$. We now have the ingredients to find the covariance of (1), which is the predictive covariance and measurement covariance as follows:

$$\boldsymbol{\Sigma}_{V,k} = \boldsymbol{\Sigma}_k + (\mathbf{I}_m \otimes \Delta\mathbf{R}_k)\,\boldsymbol{\Sigma}_{\mathbf{e}_\text{y}}\,(\mathbf{I}_m \otimes \Delta\mathbf{R}_k)^{\mathsf{T}}. \tag{11}$$

B. Solving the Pose Change Cost Function

The previous section allows us to make predictions of the magnetic field at locations after the pose change based on measurements from before the pose change to formulate the cost function in (1). However, we do not have access to the true pose change; we can estimate it up to an estimation error. To this end, we define the positional and rotational error of the estimate as $\boldsymbol{\epsilon}_k^{\mathsf{b}_k} \in \mathbb{R}^3$ and $\boldsymbol{\eta}_k^{\mathsf{b}_k} \in \mathbb{R}^3$, respectively, where we assume that both $\boldsymbol{\epsilon}_k^{\mathsf{b}_k}$ and $\boldsymbol{\eta}_k^{\mathsf{b}_k}$ are zero-mean with a Gaussian distribution. As rotations in 3-D spaces are defined in the special orthogonal group SO(3), which is part of the matrix Lie groups (for details on the Lie groups we refer the reader to [33]), there exists an

exponential map that allows us to parameterize the rotational error as $\mathbf{R}(\boldsymbol{\eta}_k^{\mathrm{b}_k})$ an orientation deviation from [10].

The cost function in (1) is a nonlinear weighted least squares problem, which can be solved using Gauss–Newton optimization [34]. To solve this, we will now find the analytical Jacobian $\boldsymbol{\mathcal{J}}_{\boldsymbol{\zeta},k}$ where we define the pose change error state by stacking the positional error and rotational error as $\boldsymbol{\zeta}_k^{\mathrm{b}_k} = \left[(\boldsymbol{\epsilon}_k^{\mathrm{b}_k})^{\mathsf{T}} \quad (\boldsymbol{\eta}_k^{\mathrm{b}_k})^{\mathsf{T}}\right]^{\mathsf{T}}$. The Jacobian $\boldsymbol{\mathcal{J}}_{\boldsymbol{\zeta},k}$ can be found by evaluating the derivative of the residual in (1) w.r.t. the error state $\boldsymbol{\zeta}_k^{\mathrm{b}_k}$, which results in

$$\boldsymbol{\mathcal{J}}_{\boldsymbol{\zeta},k} = \underbrace{\nabla_{\boldsymbol{\zeta}} \Delta\mathbf{R}_k^{\mathsf{T}} \mathbf{Y}_k^{\mathrm{b}_k}}_{\mathcal{Y}_{\boldsymbol{\zeta},k}} - \underbrace{\nabla_{\boldsymbol{\zeta}} f(\Delta\mathbf{P}_k^{\mathrm{b}_k} + \Delta\mathbf{R}_k \mathbf{S}^{\mathrm{b}_{k-1}})}_{\boldsymbol{\mathcal{F}}_{\boldsymbol{\zeta},k}} \tag{12}$$

where the operator $\nabla_{\boldsymbol{\zeta}}$ is defined to take the partial derivatives as $\nabla_{\boldsymbol{\zeta}} h(\cdot) = \left[\frac{\partial h(\cdot)}{\partial \epsilon_1} \quad \dots \quad \frac{\partial h(\cdot)}{\partial \epsilon_3} \quad \frac{\partial h(\cdot)}{\partial \eta_1} \quad \dots \quad \frac{\partial h(\cdot)}{\partial \eta_3}\right]$. To find $\mathcal{Y}_{\boldsymbol{\zeta},k}$, we make use of the small angle approximation, which allows us to parameterize the rotational error as $\mathbf{R}(\boldsymbol{\eta}) \approx (\mathbf{I} - [\boldsymbol{\eta}\times])$ [35]. Where $[\cdot\times]$ is an operator, reshaping a vector of $\in \mathbb{R}^3$ into a skew symmetric matrix $\in \mathbb{R}^{3\times 3}$, such that $[\mathbf{a}\times]\mathbf{b} = \mathbf{a} \times \mathbf{b}$. We then find $\mathcal{Y}_{\boldsymbol{\zeta},k} = \left[0_{3\ m\times 3} \quad \mathcal{Y}_{\boldsymbol{\eta},k}\right]$, where the zeros are because the derivative w.r.t. the position error $\boldsymbol{\epsilon}_k^{\mathrm{n}}$ is zero and we have $\mathcal{Y}_{\boldsymbol{\eta},k} = \left[[\Delta\mathbf{R}_k^{\mathsf{T}}\mathbf{y}_{1,k}^{\mathrm{b}_k}\times]^{\mathsf{T}}, \dots, [\Delta\mathbf{R}_k^{\mathsf{T}}\mathbf{y}_{m,k}^{\mathrm{b}_k}\times]^{\mathsf{T}}\right]^{\mathsf{T}}$.

Similar to [32], the Jacobian $\boldsymbol{\mathcal{F}}_{\boldsymbol{\zeta},k}$ of the latent function $f(\cdot)$ w.r.t. the error state $\boldsymbol{\zeta}_k^{\mathrm{n}}$ by evaluating

$$\boldsymbol{\mathcal{F}}_{\boldsymbol{\zeta},k} = \nabla_{\boldsymbol{\zeta}} \mathbf{K}_{k,k-1} \left(\mathbf{K}_{k-1,k-1} + \sigma_{\mathrm{y}}^2 \mathbf{I}_{3m}\right)^{-1} \mathrm{vec}(\mathbf{Y}_{k-1}^{\mathrm{b}_{k-1}}). \tag{13}$$

We show the derivative $\nabla_{\boldsymbol{\zeta}}\mathbf{K}$ in Appendix A. The derivative $\nabla_{\boldsymbol{\zeta}}\mathbf{K}_{k,k-1}$ becomes a tensor of shape $\mathbb{R}^{3\ m\times 6\times 3\ m}$, which after multiplication with the data part in (13) results in the derivative of the latent function $\boldsymbol{\mathcal{F}}_{\boldsymbol{\zeta},k} \in \mathbb{R}^{3\ m\times 6}$.

We can now solve the pose change in (1) using Gauss–Newton optimization. The estimation error can be found as follows:

$$\begin{bmatrix} \boldsymbol{\epsilon}_k^{\mathrm{b}_k} \\ \boldsymbol{\eta}_k^{\mathrm{b}_k} \end{bmatrix} = \left(\boldsymbol{\mathcal{J}}_{\boldsymbol{\zeta},k}^{\mathsf{T}} \boldsymbol{\Sigma}_{V,k}^{-1} \boldsymbol{\mathcal{J}}_{\boldsymbol{\zeta},k}\right)^{-1} \boldsymbol{\mathcal{J}}_{\boldsymbol{\zeta},k}^{\mathsf{T}} \boldsymbol{\Sigma}_{V,k}^{-1} \left(\Delta\hat{\mathbf{R}}_k^{\mathsf{T}} \mathbf{Y}_k^{\mathrm{b}_k} - \boldsymbol{\mu}_k)\right) \tag{14}$$

which can be used to update our estimate of the pose change as follows:

$$\begin{aligned} \Delta\hat{\mathbf{p}}_k^{\mathrm{b}_k} &\leftarrow \Delta\hat{\mathbf{p}}_k^{\mathrm{b}_k} + \boldsymbol{\epsilon}_k^{\mathrm{b}_k} \\ \Delta\hat{\mathbf{R}}_k &\leftarrow \exp_{\mathbf{R}}(\boldsymbol{\eta}_k^{\mathrm{b}_k}) \Delta\hat{\mathbf{R}}_k \end{aligned} \tag{15}$$

where $\exp_{\mathbf{R}}(\cdot)$ is an operation that maps the orientation deviation to a Rotation matrix as defined in [10]. By recursively updating (14) and (15), the cost function (1) is minimized.

C. Pose Change Algorithm for Analysis

In the previous sections, we described all the ingredients necessary to solve for the pose change $\{\Delta\mathbf{p}_k^{\mathrm{b}_k} \Delta\mathbf{R}_k\}$ and find its covariance $\boldsymbol{\Sigma}_{\boldsymbol{\zeta},k}$ in (3). For analysis, we compare the pose change covariance of three different scenarios. For the first scenario, we assume a magnetometer array as described in Section II-A, and the covariance is estimated with (3). For the second scenario, we consider a "grouped" number of magnetometers moving together, without rigid body constraints. To be more explicit, the magnetometers move the same as in the first scenario, according to (7), but the pose change covariance is estimated as follows:

$$\boldsymbol{\Sigma}_{\boldsymbol{\zeta},k}^{(2)} = \hat{\lambda}_k \left(\sum_{i=1}^{m} \boldsymbol{\mathcal{J}}_{\boldsymbol{\zeta},i,k}^{\top} \boldsymbol{\Sigma}_{V,i,k}^{-1} \boldsymbol{\mathcal{J}}_{\boldsymbol{\zeta},i,k}\right)^{-1} \tag{16}$$

where $\boldsymbol{\mathcal{J}}_{\boldsymbol{\zeta},i,k}$ and $\boldsymbol{\Sigma}_{V,i,k}$ are found by evaluating (12) and (11), respectively, for a single magnetometer i. In addition, we compare against a third scenario where we have a single magnetometer. Again, the magnetometers move according to (7), the same as in the first scenario, but the pose change covariance is estimated by taking the average of all individual magnetometers as follows:

$$\boldsymbol{\Sigma}_{\boldsymbol{\zeta},k}^{(3)} = \hat{\lambda}_k \frac{1}{m} \sum_{i=1}^{m} \left(\boldsymbol{\mathcal{J}}_{\boldsymbol{\zeta},i,k}^{\top} \boldsymbol{\Sigma}_{V,i,k}^{-1} \boldsymbol{\mathcal{J}}_{\boldsymbol{\zeta},i,k}\right)^{-1}. \tag{17}$$

We illustrate the three different scenarios in Fig. 3. We show the algorithm to estimate the pose change and covariance cases in Algorithm 1.

Algorithm 1: Nonlinear Least Squares Estimates of the Pose Change and Covariances for Scenarios 1, 2, and 3.

Input: Initial condition, Magnetometer locations, measurements $\{\Delta\mathbf{p}_{k,0}^{\mathrm{b}_k}, \Delta\mathbf{R}_{k,0}, \mathbf{S}^{\mathrm{b}_{k-1}}, \mathbf{Y}_{k-1}^{\mathrm{b}_{k-1}}, \mathbf{Y}_k^{\mathrm{b}_k}\}$.
Initialize iteration counter and stepsize $\{\tau = 0, \beta_0 = 1\}$.
while Not converged- **do**
  Compute the $\boldsymbol{\mu}_{k,\tau}$ and $\boldsymbol{\Sigma}_{k,\tau}$ from (10)
  Evaluate the cost function V_τ from (2).
  if $V_\tau > V_{\tau-1}$ **then**
    Update stepsize $\beta_\tau \leftarrow 0.5 \cdot \beta_{\tau-1}$
    Reset position change $\Delta\hat{\mathbf{p}}_{k,\tau}^{\mathrm{b}_k} \leftarrow \Delta\hat{\mathbf{p}}_{k,\tau-1}^{\mathrm{b}_k}$
    Reset orientation change $\Delta\hat{\mathbf{R}}_{k,\tau} \leftarrow \Delta\hat{\mathbf{R}}_{k,\tau-1}$.
  end if
  Compute the Jacobian from (12)
  Update pose estimate from (15)
  Update iteration counter: $\tau := \tau + 1$
end while
set $\{\Delta\hat{\mathbf{p}}_k^{\mathrm{b}_k} \leftarrow \Delta\hat{\mathbf{p}}_{k,\tau}^{\mathrm{b}_k}, \Delta\hat{\mathbf{R}}_k \leftarrow \Delta\hat{\mathbf{R}}_{k,\tau}\}$
Estimate the pose change covariances $\boldsymbol{\Sigma}_{\boldsymbol{\zeta},k}$, $\boldsymbol{\Sigma}_{\boldsymbol{\zeta},k}^{(2)}$ and $\boldsymbol{\Sigma}_{\boldsymbol{\zeta},k}^{(3)}$ from (2), (16) and (17) respectively.
Return $\{\Delta\hat{\mathbf{p}}_k^{\mathrm{b}_k}, \Delta\hat{\mathbf{R}}_k, \boldsymbol{\Sigma}_{\boldsymbol{\zeta},k}, \boldsymbol{\Sigma}_{\boldsymbol{\zeta},k}^{(2)}, \boldsymbol{\Sigma}_{\boldsymbol{\zeta},k}^{(3)}\}$

III. Analysis

We analyze the pose change precision in different simulations. First, in Section III-A, we simulate the array moving in-plane and out-of-plane with varying movement speeds, resulting in varying distances traversed by the magnetometer array during a pose change. In the remainder of the work, this will be referred to as a step distance. Second, in Section III-B, we change the size of the magnetometer array, resulting in a varying sensor separation distances between magnetometers. Next, in Section III-C, we simulate different magnetometer configurations, where we use

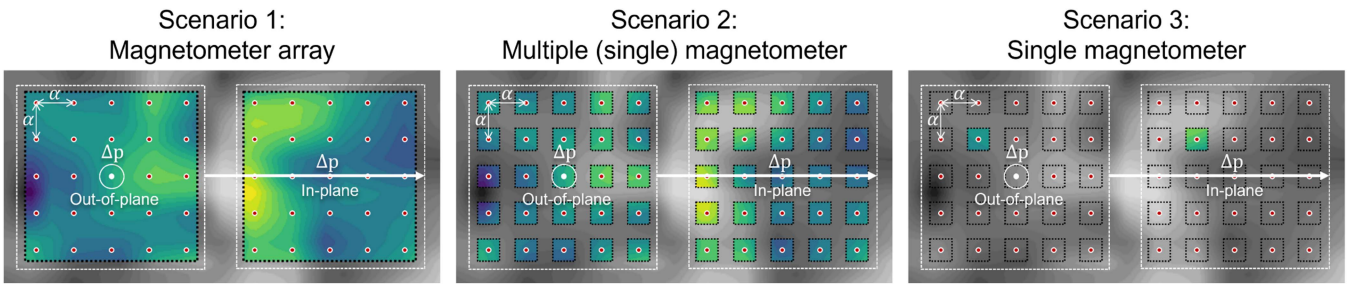

Fig. 3. Illustrative example of estimating the pose change covariance for the three scenarios. The norm of a simulated magnetic field is plotted where color indicates the amount of information used to estimate the pose change covariance. A red dot indicates a magnetometer. In all scenarios, the magnetometers move the same. The pose change covariance is estimated according to (3), (16), and (17) for scenarios 1, 2, and 3, respectively.

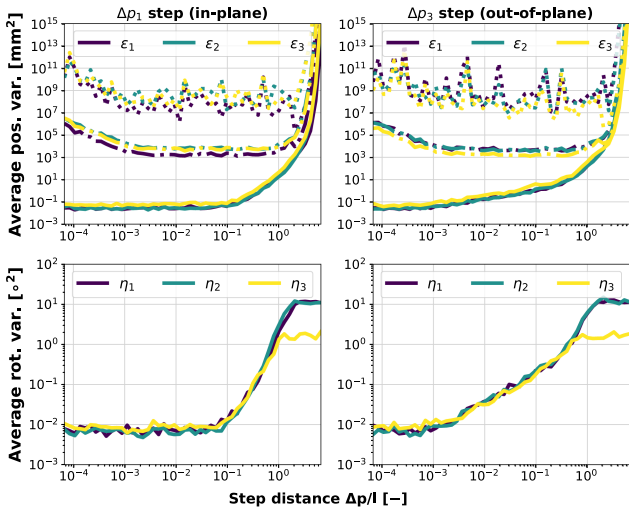

Fig. 4. Estimated average positional (top) and rotational (bottom) variance of 30 MC simulations. A square 25-magnetometer array with sensor separation distance of 37.5 mm. The array undergoes a positional change $\Delta\mathbf{p}$ in-plane (left) and out-out-plane (right) as depicted in Fig. 3. The variances are estimated in three ways, where the solid line assumes Scenario 1 uses (3), the dashed lines assume Scenario 2 with (16), and the dotted lines assume Scenario 3 with (17).

a line (1-D), a square (2-D), and a cube (3-D). Afterward, in Section III-D, we simulate the influence of the magnitude of magnetometer noise covariance leading to a varying signal to ratio (SNR). Finally, in Section III-E, we analyze how magnetometer measurement biases, positional magnetometer misalignments, and rotational magnetometer misalignments impact the pose change estimate when a magnetometer array moves in a straight line.

We use the following assumptions to create synthetic data to represent the magnetic field in simulations. We mimic the magnetic field created by the Earth in Delft, The Netherlands, which is approximately $\begin{bmatrix}19.2 & 0.8 & 45.5\end{bmatrix}^{\mathrm{T}}$ μT. On top of the simulated Earth magnetic field, we add magnetic field anomalies sampled from a GP with zero mean and the curl-free kernel from (5). We use hyperparameters $l = 0.15$ m, $\sigma_{\mathrm{f}} = 5$ μT, and $\sigma_n^2 = 0.0012$ μT, similar to those reported in [25]. For prediction, we use the same hyperparameters as for creating the synthetic data for the curl-free kernel to account for the presence of anomalies. In addition, we also use $\sigma_{\mathrm{con}} = 15$ μT in the constant kernel from (4) to account for the Earth's magnetic field.

It should be noted that a good initial estimate is necessary due to the nonconvex nature of the cost function we want to minimize. Therefore, for the first four simulations, in Sections III-A to III-D, we initialize the Algorithm 1 at the true pose change. For the final simulation in Section III-E, we initialize Algorithm 1 at zero, i.e., $\Delta\hat{\mathbf{p}}_{k,0}^{\mathrm{b}_k} = \mathbf{0}_{3\times1}$ and $\Delta\hat{\mathbf{R}}_{k,0} = \mathbf{I}_3$. All magnetometers in Sections III-A to III-D are aligned with the body frame and are assumed to have no errors besides measurement noise.

The simulations in Sections III-A to III-D compare the three different scenarios introduced in Section II-C and illustrated in Fig. 3, where scenario 1 assumes a 25-magnetometer array with pose change covariance as estimated by (3). All magnetometers for scenarios 2 and 3 undergo the same pose change, but the pose change covariances are estimated with (16) and (17), respectively. Furthermore, multiple magnetometers placed in a non-collinear configuration are needed to estimate the rotation [24], [36]. Therefore, we only estimate the rotational variance for scenarios 2 and 3.

A. Analysis on Varying the Movement Speed

Indoor localization happens at varying movement speeds and sampling frequencies, resulting in different distances traversed by the magnetometer array during a pose change, denoted as a step distance $\Delta\mathbf{p}$. In this section, we analyze the precision of the pose change estimate when moving at different speeds using a magnetometer array. To this end, we simulate a square 25-magnetometer array taking different step distances in-plane and out-of-plane directions. We generalize by making the results independent of the length-scale l by taking step distance per unit of length-scale as $\Delta\mathbf{p}_l = \Delta\mathbf{p}/l$. We show the results in Fig. 4.

For movement speeds of < 1.5 m/s, assuming a sampling rate is 100 Hz and a length-scale $l = 0.15$ m, the highest positional and rotational precision is obtained when using a magnetometer array (scenario 1). This can be seen in the in-plane direction where the positional and rotational variances from (3) in the in-plane direction are the lowest when $\Delta\mathbf{p}_l < 0.1$ at approximately 0.04 mm^2 and 0.01°^2}, respectively. We observe similar precision in the out-of-plane direction when $\Delta\mathbf{p}_l < 10^{-3}$. This effect can be attributed to the predictive quality of the curl-free kernel from (5) in our GP model, which decays with distance. This shows

that when using a magnetometer array, the highest positional precision is found when the overlap between the locations of magnetometers before and after the pose change is maximized. This can be attained by moving at slow movement speeds in the in-plane direction resulting in a step of at maximum of 10% the length-scale l, and will lead to submillimeter and subdegree pose estimation errors.

The presence of the Earth's magnetic field, which provides information on the magnetic North, provides rotational information independent of the movement speed. This effect is captured with the constant kernel in (4), of which the predictive quality does not decay with distance. This effect can be observed in Fig. 4 at big step distances $\Delta\mathbf{p}_l > 1$, where the pose change can be estimated with a yaw angle η_3 precision of at least 2°^2} and a roll angle η_1 and pitch angle η_2 precision of 10°^2}. This demonstrates that in the absence of anomalies in the magnetic field, the rotation can still be estimated with approximately a few degrees of error.

As observed in Fig. 4, a movement speed between 0.015 m/s and 15 m/s, assuming a sampling rate is 100 Hz and a length-scale $l = 0.15$ m, resulting in step distances of $10^{-3} < \Delta\mathbf{p}_l < 1$ attains the highest positional precision when using multiple single magnetometers (scenario 2). This results in positional variances of bigger than 10^3 mm^2 for ϵ_1 and 10^4 mm^2 for ϵ_2 and ϵ_3. The positional variances increase with 3 decades for a slower movement speed when $10^{-2} < \Delta\mathbf{p}_l < 10^{-1}$. The same effects are observed for the individual magnetometer (scenario 3), with positional variances approximately 6 decades higher. This clearly illustrates the benefit of using an array over single magnetometers, where at slow movement speeds resulting in step distances below $\Delta\mathbf{p}_l < 0.1$, yields in at least 6 decades lower positional variance than using multiple magnetometers and 10 decades lower than using a single magnetometer.

B. Analysis on Varying the Magnetometer Array Size

Different sizes of magnetometer arrays have been used in literature, see, e.g., [21], [24], [37]. If we build a magnetometer array, we can place the magnetometers close or far apart, leading to different array sizes. To analyze the quality of the pose change covariance from (1) under different magnetometer array sizes, we vary the sensor separation distance α. The sensor separation distance α, is the closest distance between a magnetometer and its neighbor, as illustrated in Fig. 3. The results are shown in Fig. 5. Similar to Section III-A, the results are generalized by taking the sensor separation distance per unit of length-scale as $\alpha_l = \alpha/l$.

For medium magnetometer array sizes, when $\alpha_l \approx 0.25$, or placing 4 magnetometers per unit of length-scale, the positional precision of the magnetometer array (scenario 1) is maximized where it has a positional variance of approximately 10^{-3} mm^2. When the array size shrinks, to $\alpha_l = 10^{-3}$, the positional precision decreases where the variance grows to approximately 10^{-1} mm^2. For larger sizes of magnetometer arrays, when $\alpha_l > 0.25$, the positional variance grows to approximately 10^{-3} mm^2, the same positional variance as when using multiple individual magnetometers (scenario 2). This illustrates that to maximize

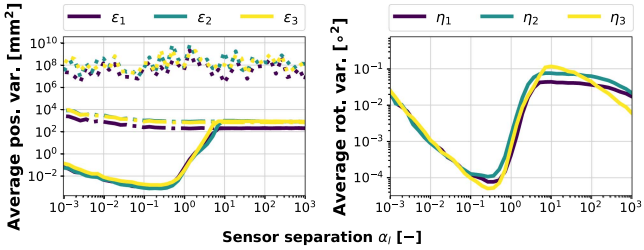

Fig. 5. Estimated average positional (left) and rotational (right) variance of 30 MC simulations. A square 25-magnetometer array with a varying sensor separation α is used. The array undergoes a step distance $\Delta\mathbf{p} = 50$ mm in-plane direction as depicted in Fig. 3. The variances are estimated in three ways, where the solid lines assume Scenario 1 with (3), the dashed lines assume Scenario 2 with (16), and the dotted lines assume Scenario 3 with (17).

the positional variance while using a magnetometer array, the sensor separation distance α between magnetometer should be maximized while the curl-free kernel from (5) in our GP model is able to make accurate predictions. In addition, placing at least four magnetometers per unit of length scale maximizes the positional precision.

Larger magnetometer array sizes lead to higher rotational accuracies, where the rotational variance decreases with a slope of -1 per decade when the sensor separation exceeds $\alpha_l > 5$. This decrease is attributed to the arm of the magnetometer s_i, which acts as a scaling factor, as seen from (7) and taking the partial derivative to obtain $\frac{\partial \mathbf{p}_i^{\mathrm{b}_k}}{\partial \boldsymbol{\eta}^{\mathrm{b}_k}} = [\Delta\mathbf{R}\mathbf{s}_i^{\mathrm{b}_k}\times]$. A local minimum in the rotational precision is found at the same magnetometer array size where the positional precision is maximized when $\alpha_l \approx 0.25$. The rotational variance drops to approximately $10^{-4^{\circ^2}}$. This shows that the bigger the magnetometer array, the higher the rotational precision. In conclusion, placing at least four magnetometers for indoor localization gives a local optimum of both rotational and positional precision.

C. Analysis on Varying the Magnetometer Configurations

In the previous simulations from Sections III-A and III-B, we have assumed that the magnetometers are placed in a square (2-D) configuration. In this simulation, we instead analyze how accurately we can estimate the position and rotation if we place magnetometers in a line (1-D), square (2-D), or cube (3-D) array using the same number of magnetometers. The magnetometers all take a step $\Delta\mathbf{p} = 50$ mm in the in-plane (p_1 direction) or out-of-plane direction (p_3 direction) from 6. The magnetometers are placed as follows: for 1-D, we place 64 magnetometers in a line, for 2-D, we place 8×8 magnetometers in a square, and for 3-D, we place $4 \times 4 \times 4$ magnetometers in a cube. The configurations are illustrated in Fig. 6. The distance between a magnetometer and its closest neighbor is the sensor separation α. We vary α to assess different sizes of the configurations. Fig. 7 shows the results. The generalization of the sensor separation distance per unit of length-scale α_l is as defined in Section III-B.

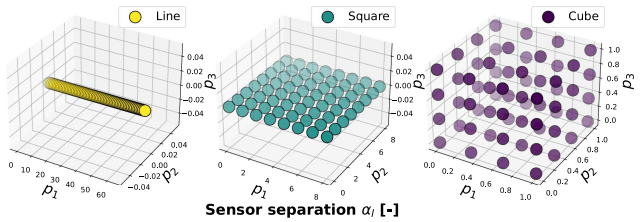

Fig. 6. Three different configurations were used in the simulation: the line configuration on the left, a square configuration in the middle, and a cube configuration on the right. The distance between a magnetometer and the closest neighbor is α. The configurations have sizes $64\alpha \times 0 \times 0$, $8\alpha \times 8\alpha \times 0$, and $4\alpha \times 4\alpha$, $\times 4\alpha$ from left to right, respectively.

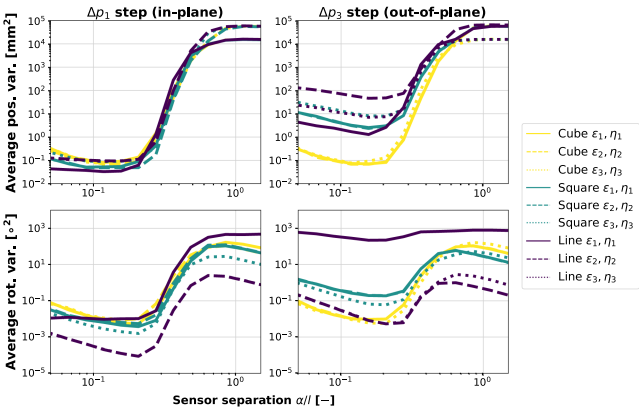

Fig. 7. Estimated average positional (left) and rotational (right) variance of 50 MC simulations. A 64-magnetometer array was used in the shape of a cube (purple), square (teal), and line (yellow), all with varying sensor separation α are used. The array undergoes a step distance $\Delta\mathbf{p} = 50$ mm in-plane direction as depicted in Fig. 3. The variances are estimated using (3).

All three configurations show similar positional accuracies when moving in-plane. However, when moving out-of-plane, the line and square configuration decrease in positional precision, where the positional variances increase by approximately a decade when $\alpha_l \approx 0.25$. In the worst case, the positional variance ϵ_2 of the line configuration increases by two decades. This shows that, depending on the degrees of freedom in movement, different configurations are desirable. When movement is restricted to be inline, e.g., a train moving along tracks from [18], the 1-D configuration results in the lowest positional variance when moving in the direction of magnetometer placement. However, when planar movement is possible, e.g., a robot moving over a flat surface from [16], the positional and rotational variances are obtained when placing the magnetometers in-plane. Similarly, when full 3-D movement is possible, e.g., movement of a human in a multistory building from [38], the lowest positional variances are obtained when placing magnetometers in all 3 spatial dimensions. In addition, the loss of precision does not weigh up if the magnetometers are placed in a plane and movement is possible out-of-plane.

The rotational precision for the cubical configuration is the same in all directions, where the rotational variances of η_1 as for η_2 and η_3 are equal, independent of the movement direction

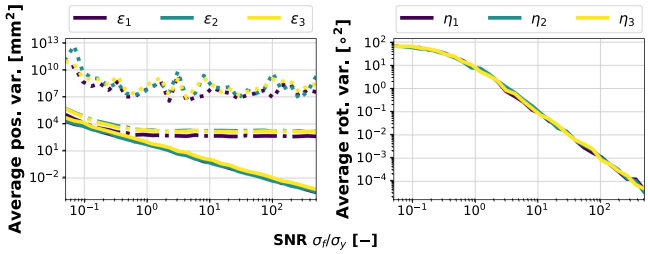

Fig. 8. Estimated average positional (left) and rotational (right) variance of 30 MC simulations. A square 25-magnetometer array with a varying magnetometer noise $\mathbf{\Sigma}_y = \sigma_y^2 \mathbf{I}_3$ is used. The array undergoes a step distance $\Delta\mathbf{p} = 50$ mm in-plane direction and has sensor separation distance $\alpha = 37.5$ mm, as depicted in Fig. 3. The variances are estimated in 3 ways, where the solid line assumes Scenario 1 with (3), the dashed lines use Scenario 2 with (16), and the dotted lines use Scenario 3 with (17).

or sensor separation α_l. The square configuration has a higher rotational precision when moving in-plane, with a rotational variance decrease of approximately half a decade in the η_3 compared to the cubical configuration. Conversely, the square configuration has a lower rotational precision when moving out-of-plane, with a rotational variance increase of approximately a decade for η_1 and η_2 compared to the cubical configuration. Finally, the line configuration shows a lower rotational variance of approximately two decades for η_2 and η_3 compared to η_1. This shows that the rotational precision can be increased by placing magnetometers orthogonal to the axis of rotation.

D. Analysis on Varying the Magnetometer Noise Levels

In practice, different grades of magnetometers are used, leading to different levels of magnetometer noise. To analyze the effects of how different magnetometer noise levels affect the pose change covariance, we simulate magnetometers with different noise levels, leading to different SNRs (σ_f/σ_y). The results are shown in Fig. 8.

For low levels of SNR, i.e., high levels of magnetometer noise, where the SNR is 0.1, the magnetometer array exhibits positional variances of approximately 10^4 mm^2, similar to using multiple individual magnetometers (scenario 2). This shows that when the magnetometer noise is high, most of the information that is added by assuming the array is subject to rigid body constraints is lost. However, with an increasing SNR, the positional precision increases as the positional variance decreases with a slope of -2 per decade. A similar trend is observed for the rotational precision, where the rotational variance decreases with a slope of -2 per decade. This shows that, contrary to single-magnetometer applications, a magnetometer array's positional and rotational precision grows proportionally to the precision of the magnetometer measurements.

E. Analysis on Varying the Magnetometer Misalignment and Measurement Bias

In the previous simulations, we have assumed the magnetometer measurements are only corrupted by measurement noise. In reality, however, magnetometers are corrupted by, among

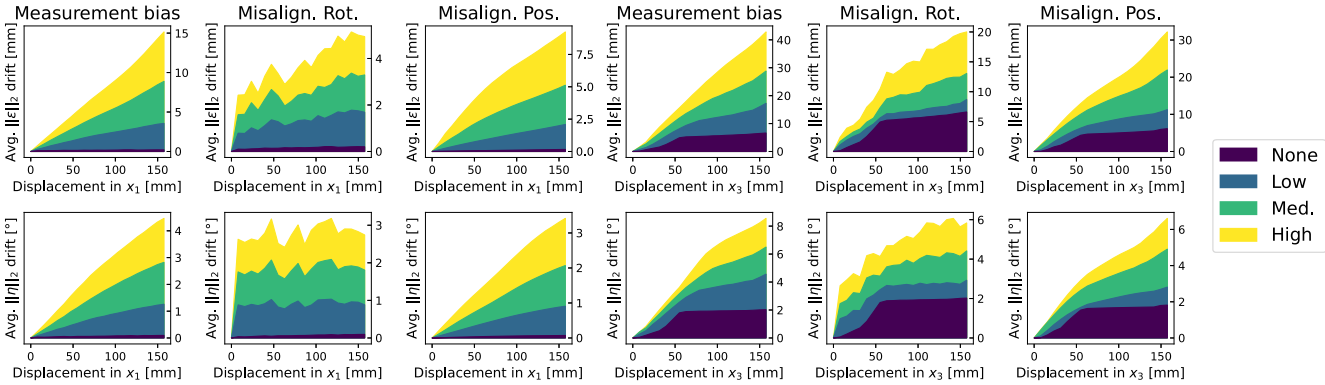

Fig. 9. Simulation results where a straight line trajectory is estimated with 3 different sources of error. The first three columns show a step $\Delta\mathbf{p} = 7.5$ mm in the-plane direction and the last three columns show a step of $\Delta\mathbf{p} = 7.5$ mm in the out-of-plane direction. In the top and bottom row, we plot the average of the 2 norms of positional errors and rotational errors, respectively, for 30 MC simulations. Synthetic data is generated from (18a) for columns 1 and 4, bias, from (18b) for columns 2 and 5, and from (18c) for columns 3 and 6.

others, calibration errors. These calibration errors will induce estimation errors. The position and rotation estimates will drift away from the true position and orientation due to an accumulation of estimation errors. We study the growth of the positional and rotational drift in the presence of different magnetometer errors. First, a magnetometer measurement bias, to simulate for magnetometer measurements not being properly calibrated. Second, a positional magnetometer misalignment to simulate when the magnetometer locations are not known exactly. Finally, a rotational magnetometer misalignment error, to simulate when the orientation of the magnetometers not known exactly. To achieve this, we simulate 4 levels with errors ranging from "None" to "High." A square 25-magnetometer array is simulated to move along a straight line in-plane and out-of-plane as depicted on the left in Fig. 3, where the magnetometer array takes 20 steps in-plane or out-of-plane with magnitude 7.5 mm. We sample bias errors per MC simulation for every magnetometer as $\mathbf{e}_{\text{bias},i,j} \sim \mathcal{N}(0, \sigma^2_{\text{bias}}\mathbf{I}_3)$, where $\sigma_{\text{bias}} = \{0.25, 0.5, 0.75\}\mu$T for $i = 1, \ldots, 25$ magnetometers and $j = 1, \ldots, 30$ MC simulations. Similarly, we sample rotational misalignment errors as $\mathbf{e}_{\text{rot},i,j} \sim \mathcal{N}(0, \sigma^2_{\text{rot}}\mathbf{I}_3)$, where $\sigma_{\text{rot}} = \{0.5, 1, 1.5\}^\circ$ and positional misalignment errors as $\mathbf{e}_{\text{pos},i,j} \sim \mathcal{N}(0, \sigma^2_{\text{pos}}\mathbf{I}_3)$, where $\sigma_{\text{pos}} = \{0.5, 1, 1.5\}$mm. The three different errors adapt measurement (6) into the three modified measurement equations from which we sample data for three separate synthetic datasets as follows:

$$\mathbf{y}^{\mathbf{b}_k}_{\text{bias},i,j,k} = f\left(\mathbf{p}^{\mathbf{b}_k}_{i,k}\right) + \mathbf{e}^{\mathbf{b}_k}_{\text{bias},i,j} + \mathbf{e}^{\mathbf{b}_k}_{i,j,k} \tag{18a}$$

$$\mathbf{y}^{\mathbf{b}_k}_{\text{rot},i,j,k} = \mathbf{R}\left(\mathbf{e}^{\mathbf{b}_k}_{\text{rot},i,j}\right) f\left(\mathbf{p}^{\mathbf{b}_k}_{i,k}\right) + \mathbf{e}^{\mathbf{b}_k}_{i,j,k} \tag{18b}$$

$$\mathbf{y}^{\mathbf{b}_k}_{\text{pos},i,j,k} = f\left(\mathbf{p}^{\mathbf{b}_k}_{i,k} + \mathbf{e}^{\mathbf{b}_k}_{\text{pos},i,j}\right) + \mathbf{e}^{\mathbf{b}_k}_{i,j,k}. \tag{18c}$$

As show in Fig. 9, when the magnetometer array moves in-plane, in the case "medium" bias errors, the positional drift accumulates to approximately 9 mm and the rotational drift accumulates to almost 3°. Similar drift is observed in the in-plane direction for a "High" positional misalignment. This shows that to minimize positional drift to less than 5% of the distance traveled and rotational drift to less than 20°/m, biases should be smaller than $0.4\mu T$, or approximately 8% of the magnetic field variations $\sigma_{\text{bias}}/\sigma_{\text{f}}$. The positional misalignments should be smaller than 1.5 mm, or 1% of the length-scale σ_{pos}/l . For a "High" rotational magnetometer misalignment error, a positional drift is observed of approximately 5 mm, and a rotational drift is seen with a maximum of approximately 3°. This shows that drift of less than 5% of the distance traveled and 20°/m can be obtained with rotational misalignment smaller than 1.5°. Higher drift is observed in the out-of-plane direction for all levels. This highlights that magnetometer placement in the direction of movement reduces drift, especially in the presence of misalignment and/or calibration errors.

IV. Experiments

Experimental data is collected by moving a 30-magnetometer array in-plane on a 0.4 m × 0.4 m square. The magnetometers are PNI RM3100, running at 100 Hz. The magnetometers on the array are ground truth position and orientation estimates are collected using an OptiTrack system. In total, six datasets are collected with two different proximities to magnetic field sources. Datasets 1–3 are recorded by sliding the array on the ground, and Datasets 4–6 are recorded by hovering the array above the ground, which leads to a total magnetic field norm range of approximately $[5, 80]$ μT and $[15, 60]$ μT, respectively, as seen at the top of Fig. 10. We use the same hyperparameters as in [25] and [29] with $l = 0.15$ m, $\sigma_{\text{lin}} = 15$ μT, $\sigma_{\text{f}} = 5$ μT, and $\sigma^2_{\text{y}} = 0.0012$ μT.

Before collecting data for the experiment, the magnetometers on the array are jointly calibrated outside, away from anomalies in the ambient magnetic field. The calibration aligns the magnetometers with the body frame and compensates for sensor-specific calibration parameters, similar to [39]. We initialize Algorithm 1 with initial conditions $\Delta\mathbf{p}^{\mathbf{b}_k}_k = 0_3$ and $\Delta\mathbf{R}_k = \mathbf{I}_3$ at every time-step k for Sections IV-A and IV-B, as in practice, we do not know the true pose change.

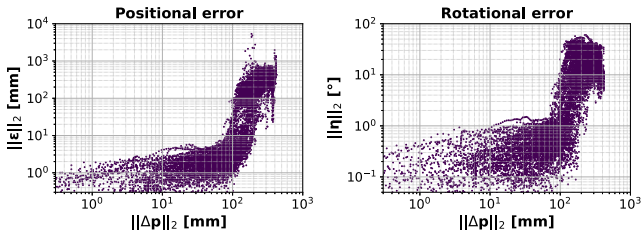

Fig. 10. Data using a 30-magnetometer array is collected moving in-plane without rotating in a $0.4\text{ m} \times 0.4\text{ m}$ square. Left and right, respectively, show the norm of the position error and orientation error. Algorithm 1 is used to estimate the pose change and is initialized with initials conditions zero. We vary the step length $\Delta\mathbf{p}$.

A. Experiment: Varying the Movement Speed

To experimentally validate the results from Section III-A, we downsample the data from the six datasets into varying step lengths in the range of $||\Delta\mathbf{p}||_2 \in [0, 0.4]$ m. We show the results in Fig. 10. For a slow movement speed, when the step length is $||\Delta\mathbf{p}||_2 < 10$ mm, all positional errors are below 4 mm, and all rotational errors are below 1°. As the movement speed increases further to a step length of $||\Delta\mathbf{p}||_2 > 50$ mm (33% of the step-length l), the positional and rotational errors increase vastly. This is closely in line with the simulation results from Section III-A, where the positional and rotational precision decreases exponentially when $\Delta\mathbf{p}_l > 0.1$, which supports the theoretical simulation results in Section III.

B. Experiment: A Short Trajectory At Ground Height

In the previous section, we validated the simulation results in Sections III-A–III-E. This section demonstrates the efficacy of using a 30-magnetometer array in estimating a full trajectory on the six datasets. We show the results in Fig. 11. We downsampled the data to 10 Hz . Although one would intuitively expect a higher sampling rate to be better, since the pose estimation errors accumulate over time, higher sampling rates lead to high positional and rotational drift. The overall trajectory the magnetometer array takes can be reconstructed well, as seen in the top row, where the estimated trajectory resembles the true square trajectory. The highest horizontal errors are in Dataset 3, with errors of approximately 90 mm in both horizontal directions at the end of the trajectory, which is approximately 1% of the horizontal distance traveled. The lowest horizontal errors are found in Dataset 4, with approximately 25 mm errors in both horizontal directions, roughly 0.5% of the horizontal traveled.

The vertical displacement p_3 drifts in every dataset, as shown in the second row, where the vertical error in Datasets 1 and 2 is approximately 25 mm at 50 s and 15 mm at 30 s, respectively. In addition, large positional oscillations occur in the vertical direction, see, e.g., where the estimated trajectory in Dataset 3 oscillates with approximately 50 mm after 40 s. This is caused by a wrong estimation of the roll and pitch angles, shown in rows 3 and 4. A constant growing drift can be observed in both the roll and the pitch angle, where the largest roll angle error is 7° at 37 s in Dataset 2, and the largest pitch angle error is approximately 3° at 50 s in Dataset 3. Finally, the yaw angle is shown in the bottom row, where the angle drift grows up to 2° at 40 s in Dataset 6. All datasets, except Datasets 1 and 3, show a rotational drift of less than 1° /m traveled. The magnetometer array provides accurate positional and rotational information, as the positional and rotational drift are mostly within one standard deviation.

Datasets 1–3, where the magnetometer array slides on the ground, show larger errors than Datasets 4–6, where the magnetometer hovers over the ground. In particular, The estimated trajectories show cyclical errors, e.g., the pitch angle of Dataset 1 where at $\{0, 10, 20, \ldots, 50\}$s, the estimated angle jumps down and up by more than 1°. These larger errors occur whenever the magnetometer array has moved a full lap and is moving over the same area. This is because we do not know the true hyper-parameters of the magnetic field, which causes larger pose estimation errors in Datasets 1-3. We also run the same algorithm on the same setup with the same trajectory, using only half the magnetometers for both halves of the magnetometer array. For this, the position errors, respectively, grow to approximately $p_1 = \{161\text{ mm}, 145\text{ mm}\}$, $p_2 = \{151\text{ mm}, -62\text{ mm}\}$, and $p_3 = \{-196\text{ mm}, -377\text{ mm}\}$ and the orientation errors accumulate to $\eta_1 = \{-19^\circ, -35^\circ\}$, $\eta_2 = \{-62^\circ, -38\}$, and $\eta_3 = \{-15^\circ, -33^\circ\}$. This shows that for good pose estimation results, the magnetometer array must measure sufficient magnetic field variations.

C. Experiment: A Long Trajectory At Knee and Hip Height

In the previous section, we showed that pose estimation with a magnetometer array performs well when close to magnetic disturbance sources. However, in practice, such strong disturbances may not be present. To evaluate performance in more realistic conditions, we study the perfomance of two trajectories in larger areas available online[1] this repository from [29], where the magnetometer array is farther away from magnetic disturbances (approximately knee heights of 0.5 m and hip height of 0.95 m). The bigger heights result in weaker magnetic field disturbances measured by the magnetometer array and thus lower magnetic field norm ranges of $[22, 32]$ μT and $[25, 31]$ μT). As the local variations are smaller compared to Section IV-B, we set $\sigma_\text{f} = 1$ μT . We apply Algorithm 1 to two datasets: "LP-1" (knee height of 0.5 m) and "NP-1" (hip height of 0.85 m). The trajectories are downsampled to 10 Hz and split into four segments (A-B, B-C, C-D, and D-E), resetting the initial pose to the ground truth at each segment's start due to growing estimation errors.

Unlike the previous experiment in Section IV-B, these results show significantly higher displacement errors due to lower SNR. Notably, horizontal displacements are estimated to be "too short"; that is, segment A-B in Fig. 12 shows the estimated rightward and downward distance traveled are only half and a quarter of the ground truth distance traveled, respectively. This effect is more pronounced in Fig. 13, where horizontal motion is barely captured. Vertical errors also increase, reaching

[1] [Online]. Available: https://github.com/Huang-Chuan/MAINSvsMAGEKF

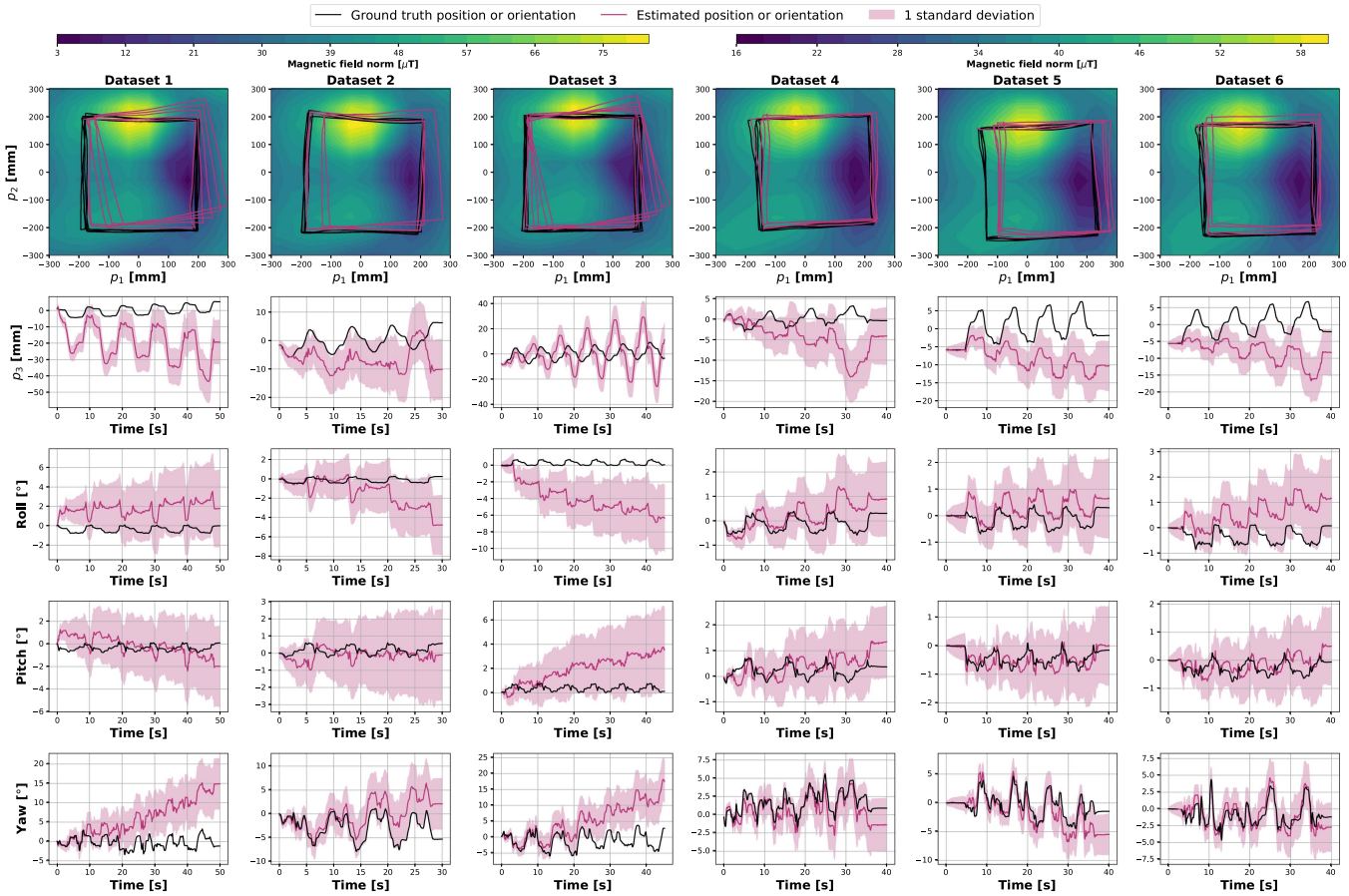

Fig. 11. Trajectory of a 30-magnetometer array moving in-plane without rotating in a 0.4 m $\times$ 0.4 m square. Datasets 1–3 are recorded by sliding the magnetometer on the ground, and Datasets 4–6 are recorded by hovering the magnetometer over the ground. The top row shows the norm of the magnetic field map in the background. Ground truth (black) and estimated (red) trajectories using Algorithm 1 and shown with one standard deviation. The top and second rows show the horizontal trajectory (in-plane) and vertical trajectory (out-of-plane) taken by the magnetometer array. The three bottom rows show the orientations.

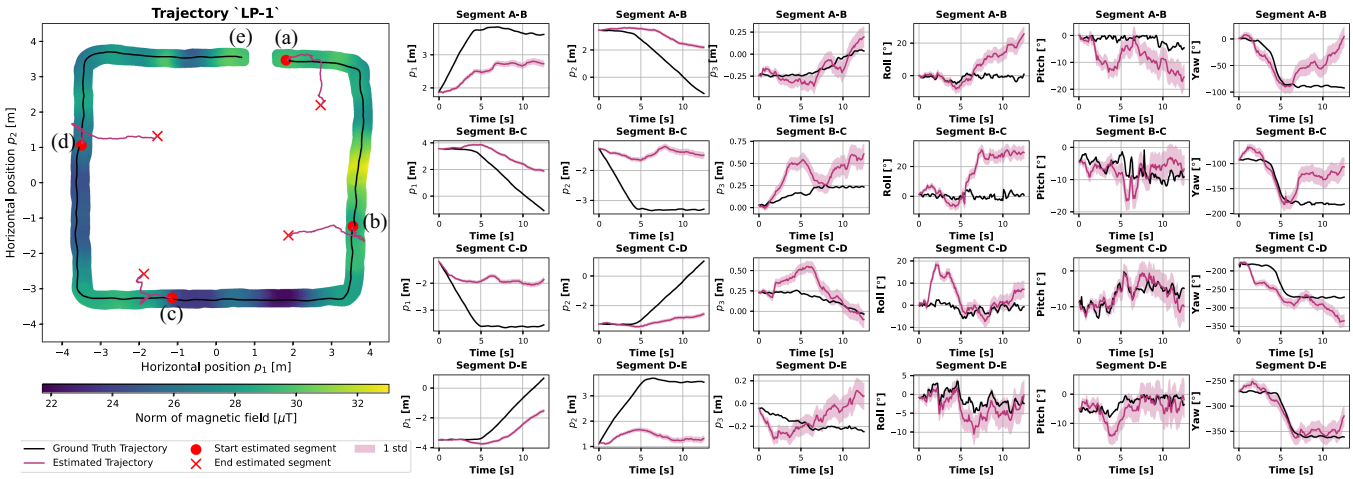

Fig. 12. Four segments of the trajectory LP-1 (approximate knee height of 0.5 m) from [29] of a 30-magnetometer array moving in-plane and rotating at the corners of a 4 m $\times$ 4 m square. Left: top-down view of the horizontal positions with the magnetic field norm in the background. Right: positions and rotations for each segment. Ground truth (black) and Algorithm 1 estimates (red) with one standard deviation.

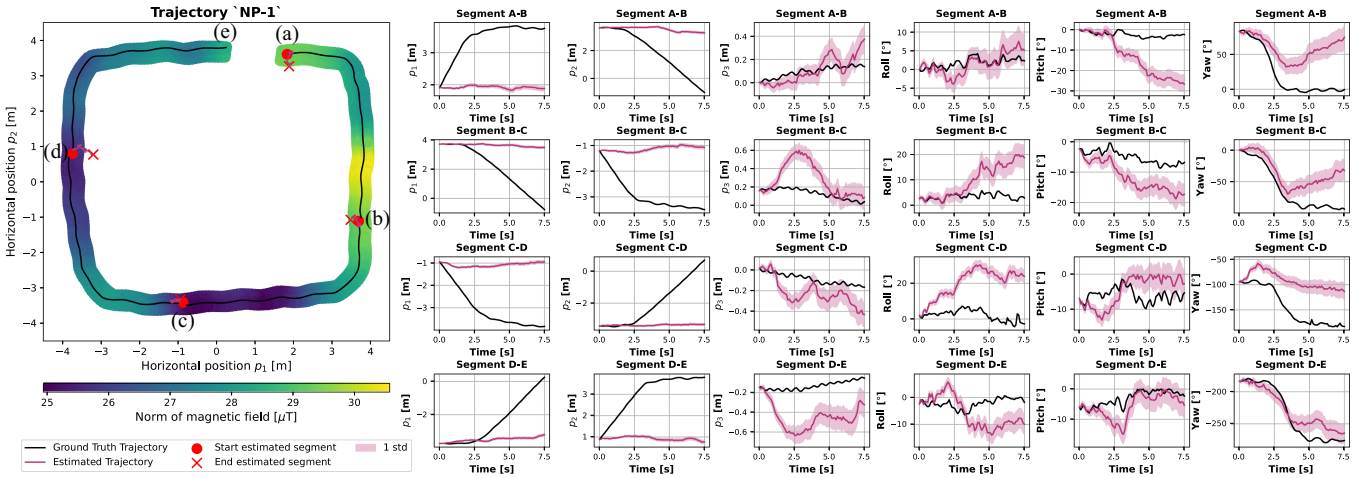

Fig. 13. Four segments of the trajectory NP-1 (approximate hip height of 0.85 m) from [29] of a 30-magnetometer array moving in-plane and rotating at the corners of a 4 m $\times$ 4 m square.Left: top-down view of the horizontal positions with the magnetic field norm in the background. Right: positions and rotations for each segment. Ground truth (black) and Algorithm 1 estimates (red) with one standard deviation.

up to approximately 0.4 m in segment B-C for both datasets. Orientation is generally estimated well, e.g., the pitch angle in segments B-C, C-D, and D-E of Fig. 12. Still, it is susceptible to large drift, as seen in Fig. 13, segment B-C, the pitch angle error grows to approximately 15°. These results show that the magnetometer array provides good orientation odometry even in areas where the magnetic field is disturbed by different sources at larger distances. It also shows that using only a magnetometer array, close proximity to magnetic disturbances is essential for accurate position odometry.

V. Conclusion

This article demonstrates the efficacy of a magnetometer array for indoor localization. We demonstrate in simulations that under sufficient magnetic field variations, the highest pose change precision is obtained at low movement speeds, i.e., when the magnetometer locations between two sets of consecutive measurements are closest to each other. We also show that when designing a magnetometer array, magnetometers should be placed in possible movement directions; for 1-D, place magnetometers in-line; for 2-D, place magnetometers in a square; and for 3-D, place magnetometers in a cube. The highest positional precision is obtained when at least four magnetometers are placed per unit of length-scale l. Although this also gives high-rotational precision, even higher precision can be obtained by placing magnetometers further apart. It should be noted that high precision can only be obtained when the overlap between the magnetometer locations of two consecutive sets of measurements is maximized, as such, magnetometers should be placed in a radius around the axis of rotation at higher rotational speeds.

We also demonstrate that to prevent a positional drift of larger than 5% of the distance traveled and a rotational drift of larger than 20°/m traveled, submillimeter positional magnetometer placement and subdegree rotational magnetometer placement precision are necessary. Similarly, magnetometer bias errors of smaller than 0.4 μT, equivalent to 8% of the magnitude of the magnetic field variations, are necessary. We demonstrate that higher quality magnetometers increase the quality of the pose estimate.

We verify the simulation results using experimental data, showing that, overall, both positions and orientations are estimated accurately if magnetic field disturbances are in close proximity to the magnetometer array. For most datasets, positional drift remains below one percent of the distance traveled, and rotational drift stays under 1°/m when the magnetometer array is close to magnetic field disturbances. However, the experiments also reveal that estimating position becomes significantly less accurate when the magnetometer array is farther away from these sources. While orientation can still be estimated reasonably well in such cases, it is susceptible to drift that increases rapidly.

The faster the movement speed, the farther away the initial estimate from the true pose change location, as a result, the optimization is more likely to get stuck in local minima. A good initial estimate can be found by using, e.g., an accelerometer and a gyroscope, sensors that frequent magnetometers. The efficacy of this is also shown in [29], which shows good results for indoor localization. An interesting direction for future research will focus on SLAM and/or calibration using the magnetometer array. Another interesting direction concerns studying the performance when magnetic field properties such as length-scales are unknown or spatially varying.

Appendix

We introduce $\kappa_{\text{se}}(\mathbf{p},\mathbf{p}') = \sigma_f^2 \exp(\frac{\|\mathbf{p}-\mathbf{p}'\|^2}{-2\,l^2})$ for notational simplicity, so that we find

$$\left.\frac{\partial \kappa_{\text{cf}}(\mathbf{p},\mathbf{p}')}{\partial \zeta_j}\right|_{\substack{\boldsymbol{\epsilon}=0_3\\ \boldsymbol{\eta}=0_3}} = \frac{a_{\epsilon_j}}{-l^2}\kappa_{\text{cf}}(\mathbf{p},\mathbf{p}') + \frac{\mathbf{A}_{\epsilon_j}}{-l^2}\kappa_{\text{se}}(\mathbf{p},\mathbf{p}') \quad (19)$$

where $j \in \{1, 2, \ldots, 6\}$ and scalars a_{ζ_j} and matrices $\mathbf{A}_{\zeta_j}$ are shown per index j below. When $j = 1, 2, 3$ we have

$$a_{\zeta_j} = (p_j - p'_j) \tag{20a}$$

$$\mathbf{A}_{\zeta_j} = (\mathbf{p} - \mathbf{p}')(\mathbf{I}_3)_{j,:} + (\mathbf{I}_3)_{:,j}(\mathbf{p} - \mathbf{p}')^\mathsf{T} \tag{20b}$$

where the notation $[\cdot]_{j,:}$ denotes the jth row and $[\cdot]_{:,j}$ denotes the jth column. Further, when $j = 4, 5, 6$ we have

$$a_{\zeta_j} = [\Delta\mathbf{R}_k \mathbf{s}_i^{\mathsf{b}_{k-1}} \times]^\mathsf{T}_{:,j}(\mathbf{p} - \mathbf{p}') \tag{21a}$$

$$\mathbf{A}_{\zeta_j} = (\mathbf{p} - \mathbf{p}') \left([\Delta\mathbf{R}_k \mathbf{s}_i^{\mathsf{b}_{k-1}} \times]_{:,j} \right)^\mathsf{T} + [\Delta\mathbf{R}_k \mathbf{s}_i^{\mathsf{b}_{k-1}} \times]_{:,j}(\mathbf{p} - \mathbf{p}')^\mathsf{T}. \tag{21b}$$

ACKNOWLEDGMENT

The authors would like to thank Gustaf Hendeby from Linköping University, and Isaac Skog and Chuan Huang from KTH Royal Institute of Technology for the collaboration to collect the experimental data used in this paper as part of the funded Swedish Research Council project 2020-04253 *Tensor-field based localization*. The authors would also like to acknowledge the ELLIIT project Visionen 2.0 for partially funding of the experimental facilities used for the data collection. This publication is part of the project "Sensor Fusion For Indoor Localization Using The Magnetic Field" with project number 18213 of the research program Veni.

REFERENCES

[1] W. Storms, J. Shockley, and J. Raquet, "Magnetic field navigation in an indoor environment," in *Proc. Ubiquitous Positioning Indoor Navigation Location Based Serv.*, 2010, pp. 1–10.

[2] R. Giuliano, F. Mazzenga, M. Petracca, and M. Vari, "Indoor localization system for first responders in emergency scenario," in *Proc. 9th Int. Wireless Commun. Mobile Comput. Conf.*, 2013, pp. 1821–1826.

[3] J. Huang, S. Junginger, H. Liu, and K. Thurow, "Indoor positioning systems of mobile robots: A review," *Robotics*, vol. 12, no. 2, 2023, Art. no. 47.

[4] T. Smieszek, G. Lazzari, and M. Salathé, "Assessing the dynamics and control of droplet-and aerosol-transmitted influenza using an indoor positioning system," *Sci. Rep.*, vol. 9, no. 1, 2019, Art. no. 2185.

[5] M. D. Rodríguez, J. Favela, E. A. Martínez, and M. A. Muñoz, "Location-aware access to hospital information and services," *IEEE Trans. Inf. Technol. Biomed.*, vol. 8, no. 4, pp. 448–455, Dec. 2004.

[6] X. Yu, G. Yang, S. Jones, and J. Saniie, "AR marker aided obstacle localization system for assisting visually impaired," in *Proc. Int. Conf. Electro/Inf. Technol.*, 2018, pp. 271–276.

[7] P. Davidson and R. Piché, "A survey of selected indoor positioning methods for smartphones," *IEEE Commun. Surv. Tut.*, vol. 19, no. 2, pp. 1347–1370, Apr.–Jun. 2017.

[8] F. Zafari, A. Gkelias, and K. K. Leung, "A survey of indoor localization systems and technologies," *IEEE Commun. Surv. Tut.*, vol. 21, no. 3, pp. 2568–2599, Jul.–Sep. 2019.

[9] G. Mendoza-Silva, J. Torres-Sospedra, and J. Huerta, "A meta-review of indoor positioning systems," *Sensors*, vol. 19, no. 20, 2019, Art. no. 4507.

[10] M. Kok, J. Hol, and T. B. Schön, "Using inertial sensors for position and orientation estimation," *Found. Trends Signal Process.*, vol. 11, no. 1-2, pp. 1–153, 2017.

[11] E. Foxlin, "Pedestrian tracking with shoe-mounted inertial sensors," *IEEE Comput. Graph. Appl.*, vol. 25, no. 6, pp. 38–46, Nov./Dec. 2005.

[12] A. Dammann, B. Siebler, and S. Sand, "Cramér–Rao lower bound for magnetic field localization around elementary structures," *Sensors*, vol. 24, no. 8, 2024, Art. no. 2402.

[13] B. Li, T. Gallagher, A. G. Dempster, and C. Rizos, "How feasible is the use of magnetic field alone for indoor positioning?," in *Proc. Int. Conf. Indoor Positioning Indoor Navigation*, 2012, pp. 1–9.

[14] B. Siebler, S. Sand, and U. D. Hanebeck, "Bayesian Cramér-Rao lower bound for magnetic field-based localization," *IEEE Access*, vol. 10, pp. 123080–123093, 2022.

[15] M. Angermann, M. Frassl, M. Doniec, B. J. Julian, and P. Robertson, "Characterization of the indoor magnetic field for applications in localization and mapping," in *Proc. Int. Conf. Indoor Positioning Indoor Navigation*, 2012, pp. 1–9.

[16] A. Solin, M. Kok, N. Wahlström, T. B. Schön, and S. Särkkä, "Modeling and interpolation of the ambient magnetic field by Gaussian processes," *IEEE Trans. Robot.*, vol. 34, no. 4, pp. 1112–1127, Aug. 2018.

[17] F. Viset, R. Helmons, and M. Kok, "An extended Kalman filter for magnetic field SLAM using Gaussian process regression," *Sensors*, vol. 22, no. 8, 2022, Art. no. 2833.

[18] B. Siebler, O. Heirich, S. Sand, and U. Hanebeck, "Joint train localization and track identification based on earth magnetic field distortions," in *Proc. IEEE/ION Position, Location Navigation Symp.*, 2020, pp. 941–948.

[19] D. Vissière, A. Martin, and N. Petit, "Using distributed magnetometers to increase IMU-based velocity estimation into perturbed area," in *Proc. 46th Conf. Decis. Control*, 2007, pp. 4924–4931.

[20] E. Dorveaux and N. Petit, "Presentation of a magneto-inertial positioning system: Navigating through magnetic disturbances," in *Proc. Int. Conf. Indoor Positioning Indoor Navigation*, 2011, pp. 1–11.

[21] E. Dorveaux, T. Boudot, M. Hillion, and N. Petit, "Combining inertial measurements and distributed magnetometry for motion estimation," in *Proc. Amer. Control Conf.*, 2011, pp. 4249–4256.

[22] C. I. Chesneau, M. Hillion, and C. Prieur, "Motion estimation of a rigid body with an ekf using magneto-inertial measurements," in *Proc. Int. Conf. Indoor Positioning Indoor Navigation*, 2016, pp. 1–6.

[23] M. Zmitri, H. Fourati, and C. Prieur, "BiLSTM network-based extended Kalman filter for magnetic field gradient aided indoor navigation," *IEEE Sensors J.*, vol. 22, no. 6, pp. 4781–4789, Mar. 2022.

[24] I. Skog, G. Hendeby, and F. Gustafsson, "Magnetic odometry-a model-based approach using a sensor array," in *Proc. 21st Int. Conf. Inf. Fusion*, 2018, pp. 794–798.

[25] I. Skog, G. Hendeby, and F. Trulsson, "Magnetic-field based odometry - an optical flow inspired approach," in *Proc. Int. Conf. Indoor Positioning Indoor Navigation*, 2021, pp. 1–8.

[26] T. Edridge and M. Kok, "Mapping the magnetic field using a magnetometer array with noisy input Gaussian process regression," in *Proc. 26th Int. Conf. Inf. Fusion*, 2023, pp. 1–7.

[27] M. Zmitri, H. Fourati, and C. Prieur, "Magnetic field gradient-based EKF for velocity estimation in indoor navigation," *Sensors*, vol. 20 no. 20, 2020, Art. no. 5726.

[28] C. Huang, G. Hendeby, and I. Skog, "A tightly-integrated magnetic-field aided inertial navigation system," in *Proc. 25th Int. Conf. Inf. Fusion*, 2022, pp. 1–8.

[29] C. Huang, G. Hendeby, C. Prieur, H. Fourati, and I. Skog, "MAINS: A magnetic field aided inertial navigation system for indoor positioning," *IEEE Sensors J.*, vol. 24, no. 9, pp. 15156–15166, May 2024.

[30] S. M. Kay, *Fundamentals of Statistical Signal Processing: Estimation Theory*. Englewood Cliffs, NJ, USA: Prentice-Hall, Inc., 1993.

[31] N. Wahlström, M. Kok, T. B. Schön, and F. Gustafsson, "Modeling magnetic fields using Gaussian processes," in *Proc. Int. Conf. Acoust., Speech, Signal Process.*, 2013, pp. 3522–3526.

[32] C. Williams and C. Rasmussen, "Gaussian processes for regression," *Adv. Neural Inf. Process. Syst.*, vol. 8, pp. 514–520, 1995.

[33] T. D. Barfoot. *State Estimation for Robotics*. Cambridge, U.K.: Cambridge Univ. Press, 2024.

[34] F. Gustafsson, *Statistical Sensor Fusion*. Lund, Sweden: Studentlitteratur, 2010.

[35] J. Sola, "Quaternion kinematics for the error-state Kalman filter," 2017, *arXiv:1711.02508*.

[36] E. Dorveaux, "Magneto-inertial navigation: Principles and application to an indoor pedometer," Ph.D. thesis, École Nationale Supérieure des Mines de Paris, Paris, France, 2011.

[37] I. Skog, J. Jaldén, J. Nilsson, and F. Gustafsson, "Position and orientation estimation of a permanent magnet using a small-scale sensor array," in *Proc. Int. Instrum. Meas. Technol. Conf.*, 2018, pp. 1–5.
[38] M. Kok and A. Solin, "Scalable magnetic field SLAM in 3D using Gaussian process maps," in *Proc. 21st Int. Conf. Inf. Fusion*, 2018, pp. 1353–1360.
[39] M. Kok and T. B. Schön, "Magnetometer calibration using inertial sensors," *IEEE Sensors J.*, vol. 16, no. 14, pp. 5679–5689, Jul. 2016.

Thomas Edridge (Graduate Student Member, IEEE) received the B.Sc. degree in mechanical engineering in 2018 and the M.Sc. degree in mechanical engineering in 2020 from the Delft University of Technology, Delft, The Netherlands, where he is currently working toward the Ph.D. degree in probablistic machine learning.

His research interests are probabilistic sensor fusion, machine learning, and indoor localization.

Manon Kok received the dual M.Sc. degrees in philosophy of science, technology, and society and in applied physics from the University of Twente, Enschede, The Netherlands, in 2007 and 2009, respectively, and the Ph.D. degree in automatic control from Linköping University, Linköping, Sweden, in 2017.

From 2009 to 2011, she was a Research Engineer with Xsens Technologies. From 2017 to 2018, she was a Postdoctoral with the Computational and Biological Learning Laboratory, University of Cambridge, U.K. She is currently an Associate Professor with the Delft Center for Systems and Control, Delft University of Technology, Delft, The Netherlands. Her research interests include probabilistic inference for sensor fusion, signal processing, and machine learning.